photonics

MDPI

Article

All-Fiber Photoacoustic Gas Sensing with Interferometric Location

Meng Li [1,2], Mengpeng Hu [1,2], Hui Zhang [1,2], Jianing Wang [3], Tongyu Tang [4], Mai Hu [1] and Qiang Wang [1,2,*]

[1] State Key Laboratory of Applied Optics, Changchun Institute of Optics, Fine Mechanics and Physics, Chinese Academy of Sciences, Changchun 130033, China; limeng203@mails.ucas.ac.cn (M.L.); humengpeng19@mails.ucas.ac.cn (M.H.); zhanghui195@mails.ucas.ac.cn (H.Z.); humai@ciomp.ac.cn (M.H.)
[2] University of Chinese Academy of Sciences, Beijing 100049, China
[3] Space Optics Department I, Changchun Institute of Optics, Fine Mechanics and Physics, Chinese Academy of Sciences, Changchun 130033, China; wangjn@ciomp.ac.cn
[4] Department of Gastroenterology, First Hospital of Jilin University, Changchun 130021, China; tangty@jlu.edu.cn
* Correspondence: wangqiang@ciomp.ac.cn; Tel.: +86-0431-86176199

Abstract: Photoacoustic spectroscopy (PAS) is a promising gas detection technique with high sensitivity, fast response, and good stability. Frequency-modulated continuous-wave (FMCW) interferometry offers precise distance detection with high spatial resolution. The combination of PAS and FMCW may lead to an optical technique for the simultaneous extraction of gas concentration and location information. Herein, we demonstrate this technique in an all-fiber sensing system by blending a fiber-pigtailed PAS sensor with an FMCW interferometer. As an example, we have measured the methane concentration and location by employing time-division multiplexing, showing a minimum detection limit of 28 ppm and a spatial resolution of 3.87 mm over a distance of ~4.9 m. This study enables the realization of a versatile technique for multiparameter gas sensing in gas leakage detection and gas emission monitoring.

Keywords: photoacoustic spectroscopy; frequency-modulated continuous-wave; time-division multiplexing; frequency-sampling method; methane

Citation: Li, M.; Hu, M.; Zhang, H.; Wang, J.; Tang, T.; Hu, M.; Wang, Q. All-Fiber Photoacoustic Gas Sensing with Interferometric Location. *Photonics* **2022**, *9*, 546. https://doi.org/10.3390/photonics9080546

Received: 9 July 2022
Accepted: 30 July 2022
Published: 3 August 2022

1. Introduction

Air pollution and gas safety have been garnering ever-increasing attention in industrial production and daily life. In recent years, accidents such as human poisoning caused by the leakage of carbon monoxide gas in coal mine production, chemical plant explosions caused by the leakage of explosive gas, and fire caused by the leakage of natural gas pipelines have occurred frequently. Therefore, it is of great significance to achieve highly sensitive gas detection and to identify its location precisely.

Photoacoustic spectroscopy (PAS), a promising technique for trace gas sensing, has unique advantages of zero background and large dynamic range. In recent decades, researchers have been committed to the development of trace gas detection using PAS and have developed cutting-edge methods to improve its performance, such as quartz-enhanced photoacoustic spectroscopy (QEPAS) [1–4] and cantilever-enhanced photoacoustic spectroscopy (CEPAS) [5], which can achieve detection sensitivity at ppb or even sub-ppt levels [6]. PAS has also been claimed to be capable of long-distance or distributed detection. Z. Gong et al. proposed an all-light and highly sensitive resonant photoacoustic sensor for remote trace methane (CH_4) detection, with a minimum detection limit as low as 15.9 ppb [7]. Y. Ma et al. reported a distributed fiber evanescent wave gas sensor based on QEPAS, which realized the detection of gas concentration in three tapered regions within 3 km, and the minimum detection limit for acetylene was 13 ppm [8]. The system stability and response time have been further enhanced by using beat-frequency technique for real-time system parameter calibration [9,10] or by locking laser wavelength to the absorption transitions [11,12]. PAS also has the ability to detect different kinds of gas

simultaneously with a dual-resonator structural cell [13]. Although the above studies on PAS can obtain sufficient sensitivity in remote detection, locating the target gas still remains an unsolved challenge in practical applications.

Currently, optical time domain reflectometry (OTDR) [14] and optical frequency domain reflectometry (OFDR) [15] are widely used in security monitoring by distributed sensing because of its remarkable advantages of anti-electromagnetic interference, anti-corrosion, and wide measurement range. OTDR has been commonly used to study the distributed measurement of hydrogen [16], methane [17], acetylene [18,19], etc. OFDR, also known as frequency-modulation continuous-wave (FMCW), exhibits not only a much higher sensitivity and spatial resolution over OTDR but also a wider dynamic range [20], which offers a promising prospect in optical sensing. In 2000, G. Stewart et al. proposed an absorption measurement method based on FMCW, which realized the effective detection of methane [21]. In 2009, F. Ye et al. applied frequency-shifted interferometry and placed multiple gas sensors along a single optical fiber to measure different gases in the case of spectral overlap, and achieved a minimum detectable acetylene concentration of 230 ppm [22]. In 2018, X. Lou et al. presented a novel method based on optical FMCW interferometry that realized simultaneous measurement of absorption spectrum and optical path length in a multipass cell [23]. Recently, they reported distributed multipoint spectral gas sensing, achieving a spatial resolution of 30 cm over a distance of 52 m and a detection limit of 55 ppm for acetylene [24].

In this study, we demonstrate the measurement of gas concentration and location in a compact setup. An all-fiber PAS gas sensor is developed, omitting the critical demand for complex and accurate optical alignment. The optical path is fully shared by an FMCW interferometer, allowing the flexibility of placement without more complex sensing apparatus. In the experiment, we chose CH_4 as the example gas. With the operation parameters optimized, photoacoustic signal and interference signal were obtained successively using time-division multiplexing for simultaneous gas concentration and location detection. A minimum detection limit of 28 ppm and spatial resolution of 3.87 mm were achieved.

2. Methodology

2.1. PAS Gas Sensing

PAS is an indirect absorption spectroscopic technology based on the photoacoustic effect. When the laser is in resonance with a particular absorption transition, a fraction of ground-state gas molecules are excited to higher energy levels due to light absorption. The subsequent nonradioactive relaxation generates localized heat of the laser beam. Then, a pressure wave is concomitantly generated with the periodically modulated laser, which can be converted into an electrical signal by an acoustic sensor, e.g., by a microphone. The amplitude of the photoacoustic signal can be expressed as [25,26]

$$S_{PA} = S_m C_{cell} \alpha P_s C, \quad (1)$$

where S_m is the microphone sensitivity, C_{cell} is the photoacoustic cell constant, α is the gas absorption coefficient, P_s is the incident laser power, and C is the gas concentration. This equation reveals that the gas concentration is proportional to the amplitude of the photoacoustic signal. Therefore, the gas concentration information can be easily retrieved from the photoacoustic signal.

2.2. FMCW Laser Ranging

The principle of Mach–Zehnder (M-Z)-based FMCW interferometry has been well documented in previous studies [27–29]. Here, only a brief overview is presented to clarify the nomenclature and parameters. A sawtooth driven laser is divided into two parallel beams, for distance measurement and reference, respectively, by one fiber coupler. Another fiber coupler recombines the two beams to form a measurement interferometer.

The interference signal is picked up by a photodetector and then fast Fourier transformed (FFT) to extract the distance as

$$L_m = \frac{cf_I T}{n_f B}, \tag{2}$$

where c is the light speed in vacuum, f_I is the oscillation frequency of the interference signal, T is the modulation period of sawtooth waveform, n_f is the group refractive index along the optical fiber, and B is the tuning range of the optical frequency sweep. When the interference signal is sampled in one period of sawtooth waveform, the spatial resolution of the system can be obtained as

$$\delta_L = \frac{c}{n_f B}. \tag{3}$$

In practical application, the wavelength of a diode laser usually exhibits a nonlinear response to injection current [30], which can cause spectrum distortion in the radio-frequency domain and thus inaccurate distance measurement. Hence, another M-Z interferometer with known length, as an auxiliary interferometer, is introduced to form a dual-interferometer ranging system. The nonlinearity can thus be corrected by frequency-sampling [29,31]. The laser emission enters the auxiliary interferometer and the measurement interferometer synchronously through the coupler, generating auxiliary interference signal $I_a(f)$ and measurement interference signal $I_m(f)$ as

$$I_a(f) = A_a \cos(2\pi f \tau_a) = A_a \cos(2\pi(f_0 + \Delta f)\tau_a), \tag{4}$$

$$I_m(f) = A_m \cos(2\pi f \tau_m) = A_m \cos(2\pi(f_0 + \Delta f)\tau_m), \tag{5}$$

where τ_a, τ_m and A_a, A_m are the time delay and the amplitude of the auxiliary interference signal and the measurement interference signal, respectively, f is the instantaneous frequency of the laser, f_0 is the initial frequency of the laser, and Δf is the frequency change of the laser. When the auxiliary interference signal is used as a clock signal to resample the measurement interference signal, the phase difference between any two adjacent extreme points is π, i.e., $2\pi\Delta f\tau_a = n\pi$, where n is an integer. The resampled measurement interference signal can be written as

$$I_m(n) = A_m \cos(2\pi f_0 \tau_m + \pi n \tau_m/\tau_a), n = 1, 2, \cdots N, \tag{6}$$

where N is the number of extreme points of the auxiliary interference signal. The radio-frequency spectrum of the resampled measurement interference signal is obtained by FFT. We suppose P is the value of abscissa corresponding to the peak point in the radio-frequency spectrum and L_a is the distance of the auxiliary interferometer. Then, the distance of the measurement interferometer after correction is retrieved as

$$L_m = \frac{PL_a}{N}. \tag{7}$$

2.3. Absorption Line Selection and Laser Characterization

A DFB laser with near infrared emission is preferred as the excitation source due to its low cost, compact size, and convenient tunability. Since the main spectral interference may come from CO_2 and H_2O, which are the important components of air, the spectral absorption simulations between 6038 cm^{-1} to 6050 cm^{-1} are performed using the HITRAN database with CH_4 (100 ppm), CO_2 (500 ppm), and H_2O (3%), as shown in Figure 1. The absorption line located at 6046.95 cm^{-1} has the strongest absorption and negligible interference, which determines the target absorption line.

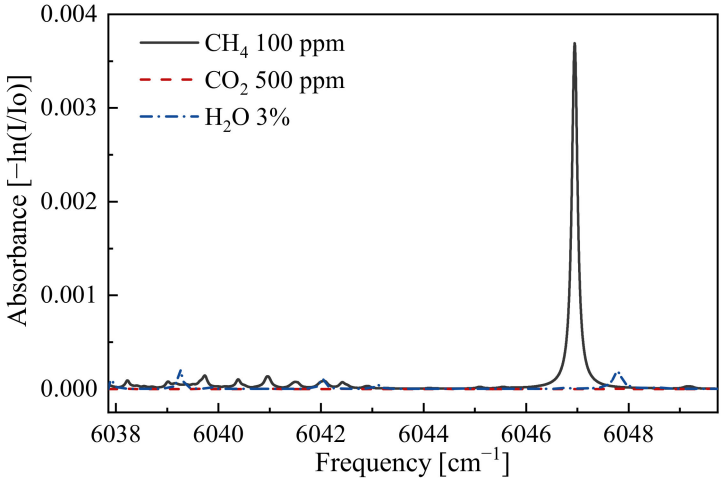

Figure 1. Absorption spectra of CH_4, CO_2, and H_2O based on HITRAN database.

The DFB laser tuning range covers the selected CH_4 absorption line with the laser temperature set at 20 °C. The emission wavelength as a function of driving current is calibrated. The current ranges from 20–150 mA with an interval of 10 mA and the wavelength is obtained using a commercial wavelength meter (671B, Bristol) with its results shown in Figure 2. A third-order polynomial fitting is performed to describe the relationship.

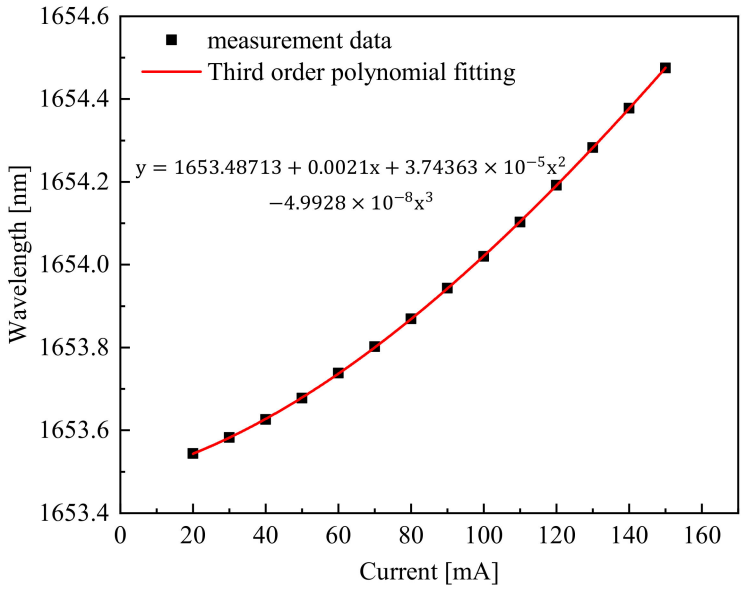

Figure 2. DFB laser wavelength as a function of driving current at 20 °C.

3. Experimental Setup

Figure 3 shows the schematic diagram of the all-fiber photoacoustic sensor with dual M-Z interferometer. The DFB laser (NLK1U5FAAA, NEL) with a center wavelength of 1653.74 nm is selected as the laser source. The time-division multiplexing method is adopted to achieve successive gas concentration measurement and ranging. For ranging, the laser scans from 1653.5437 nm to 1654.1919 nm (6045.2478–6047.6176 cm^{-1}) by applying a 1 Hz sawtooth signal to the injection current. According to Equation (3), we expect the ideal spatial resolution to be as small as 2.88 mm. The laser is divided into two beams by coupler 1 and 90% of the laser power is allocated to the measurement interferometer. Then, the light entering the measurement interferometer is divided into a reference arm and a measurement arm through coupler 3, and the measurement interference signal is generated at coupler 5. The other 10% of the laser power is allocated to the auxiliary interferometer

with an optical path difference of 12 m, which is used to generate a trigger to resample the measurement interference signal. According to Nyquist sampling law, the optical path difference of the auxiliary interferometer is required to be at least 2 times longer than the measurement interferometer. To ensure synchronous sampling, photodetectors 1 and 2 (PDA20CS2, Thorlabs) of the same type are selected to extract the measurement interference signal and the auxiliary interference signal, respectively. A commercial data acquisition card (USB-6356, NI) is used to digitize the interference signals at a sampling rate of 1 MS/s.

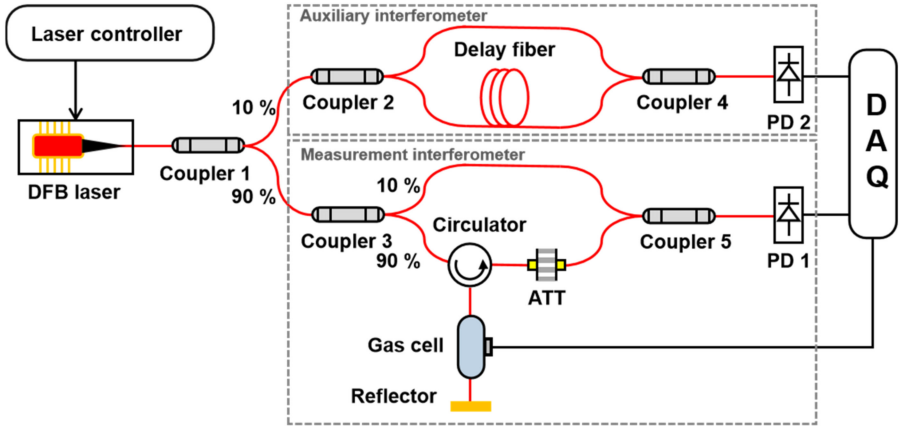

Figure 3. Experimental setup of the all-fiber PAS system with interferometric location. DFB laser, distributed feedback laser; Coupler 1 and Coupler 3, 90:10; Coupler 2, Coupler 4, and Coupler 5, 50:50; ATT, optical attenuator; PD, photodetector; DAQ, data acquisition card.

For gas concentration detection, the laser scans across the absorption transition of CH_4 by superimposing the 1 Hz sawtooth waveform on a high-frequency sinusoidal modulation. A fiber-pigtailed PAS cell is inserted in one beam of the measurement interferometer via an optical fiber circulator. The other end of the cell is spliced to one reflector with a reflectivity of more than 95%. This reflector acts as a booster to amplify the photoacoustic signal by enhancing the laser power, and as a marker for PAS cell location. Here, as a proof-of-principle demonstration, we adopt a one-dimensional longitudinal tube as the PAS cell. The PAS cell consists of an acoustic resonator (ϕ 3 $\times$ 35 mm), two buffers (ϕ 12 $\times$ 17.5 mm), and a miniature electret microphone (EK-23024, Knowles Electronics). The gas inlet and outlet are in the middle of each buffer. A standing acoustic wave is formed in the PAS cell to enhance the acoustic signal as the laser scans across the gas absorption feature. Then, the acoustic signal is detected by the microphone and converted to a voltage signal [11,32]. The electrical signal is demodulated by a lock-in amplifier with a filter slop of 12 dB/oct and a time constant of 30 ms to obtain the photoacoustic signal. A short micro-nanofiber is used to omit complicated optical alignment. Its diameter is fabricated as ~1 µm by a fused tapering technique [8,33] and the power ratio of the evanescent field is expected to be as high as 25%.

4. Experimental Results

4.1. Optimization of Experimental Parameters

For resonant PAS, the response reaches the maximum when the modulation frequency matches the resonant frequency of the PAS cell. The relationship between modulation frequency and PAS signal was experimentally calibrated. Pure N_2 was used to empty the air before the PAS cell was filled with a 1% CH_4 gas sample. By adjusting the modulation frequency from 1900 Hz to 3300 Hz, the PAS signal in its second harmonic ($2f$) manner was recorded as shown in Figure 4. The highest PAS signal amplitude was obtained at the modulation frequency of 2.4 kHz. In the following experiments, the sinusoidal modulation frequency of the laser was set to 2.4 kHz.

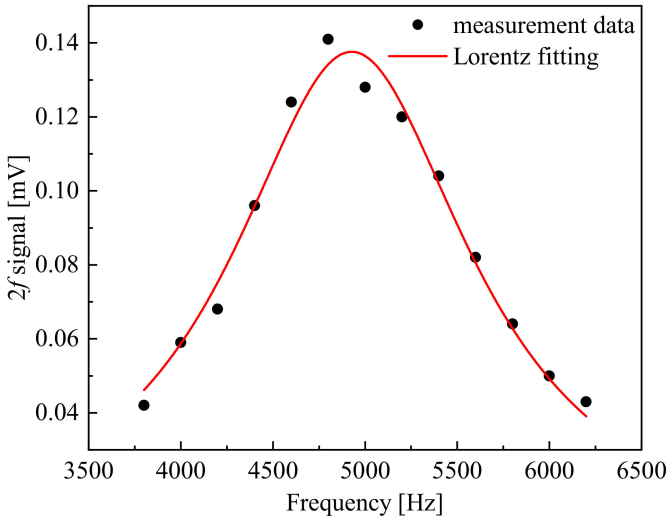

Figure 4. Frequency response of the photoacoustic cell. The data can be fitted well by a Lorentz fitting.

The PAS response also depends on the modulation depth of the laser, which needs to be optimized to improve the detection sensitivity. Using 1% CH_4 calibrated gas, the experiment was conducted at varied modulation currents from 2.5 to 20 mA. Figure 5 shows the 2*f* signal response to the modulation current, yielding the optimized modulation current of 11.25 mA to aid in gas concentration sensing implementation.

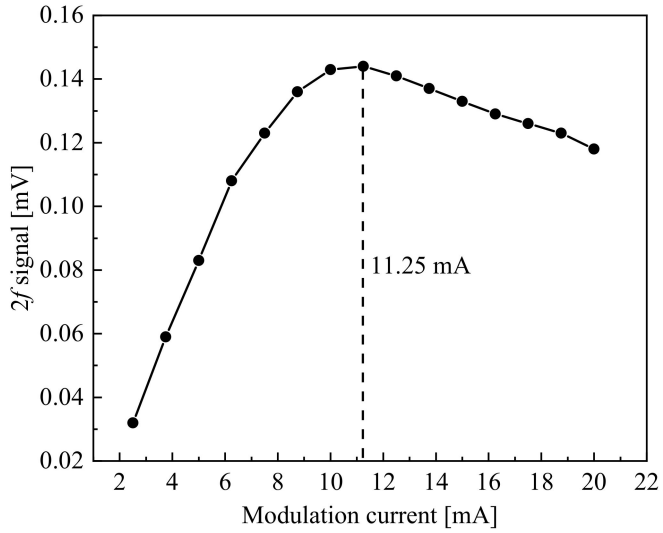

Figure 5. The 2*f* signal of CH_4 under different modulation currents.

4.2. Gas Concentration Sensing

With the optimal experimental parameters optimized, different CH_4/N_2 gas mixtures with known concentration were introduced into the gas chamber to investigate the gas concentration sensing performance. The concentration of the gas mixture was adjusted to 900 ppm, 2000 ppm, 4000 ppm, 6000 ppm, 8000 ppm, and 1%, successively, using a commercial gas dilution instrument (SONIMIX 7100, LNI Swissgas, Versoix, Switzerland). Figure 6a depicts the 2*f* signals of different concentrations. The amplitude of the 2*f* signal as a function of concentration is plotted in Figure 6b, where each point represents the averaged peak value. In addition, each error bar shows the standard deviation from 20 measurements. An excellent linear response has been achieved between the CH_4 concentration and the peak value of the 2*f* signal, which is further confirmed by performing linear fitting with an R-square value of 0.999.

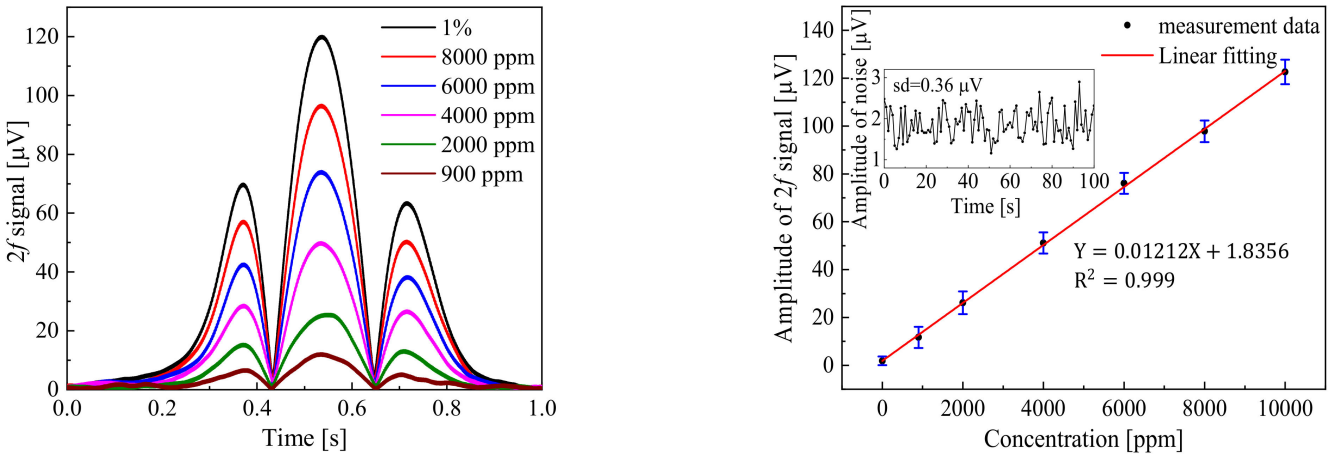

Figure 6. (**a**) The 2*f* signal with different concentrations of CH_4/N_2 mixture; (**b**) linear relationship between 2*f* signal and CH_4 concentration. Inset: noise under N_2 background. Each error bar is the standard deviation from 20 measurements and the magnitudes of the error bars are scaled up by 5-fold for clarity.

To determine the minimum detectable concentration of the sensor, high pure N_2 was introduced into the PAS cell for noise evaluation of about 100 s. The illustration in Figure 6b shows the experimental result. The standard deviation of the noise is about 0.36 μV, resulting in a signal-to-noise ratio of 32 corresponding to 900 ppm CH_4. Therefore, the sensor has achieved a detection limit of 28 ppm. With incident power of 4.42 mW and detection bandwidth of 5 Hz, a normalized noise equivalent absorption (NNEA) coefficient of 1.98×10^{-8} $cm^{-1} \cdot W \cdot Hz^{-1/2}$ is obtained.

4.3. Laser Ranging

The original interference signals of the auxiliary interferometer and measurement interferometer are shown in Figure 7a,b, respectively. The increased interference signal amplitude with time derives from the diode laser, whose emission intensity scales with the driving current. In the frequency-resampling implementation, extreme points of the auxiliary interference signal were used to resample the measurement interference signal. We employed the Hanning window function digital band-pass filter and wavelet threshold denoising method to mitigate the fake extreme points. Figure 7c illustrates the processed interference signal from that shown in Figure 7a. The obvious burst signal is attributed to the denoising process and the following unevenly spaced interference derives from the mode hopping of the DFB laser, which would deteriorate the ranging accuracy [31,34] and was deleted before performing frequency-resampling. At the exact time of each extreme point of the denoised auxiliary interference signal, the filtered signal from the measurement interferometer was resampled. Figure 7d depicts the resampled measurement interference signal with equal optical frequency intervals. In Figure 7, to show the signal characteristics more clearly, we only demonstrate interference signals for 0.1 s.

Figure 8a illustrates the entire distance spectrum, which was interpolated by zero-filling the resampled signal in the time domain. The inset, for comparison, shows the distance spectrum before applying the frequency-resampling and filter processing. It is obvious that the resampled distance spectrum has a much higher signal-to-noise ratio. This is because the noise of the original interference, including high-frequency noise, low-frequency noise, and Gaussian white noise shown in Figure 7a,b, can substantially affect the measurement accuracy and precision of laser ranging with the spectrum broadening in the radio-frequency domain [35,36]. Figure 8b shows the magnification of the distance spectrum from 4.89 m to 4.94 m. The spatial resolution, defined as the full width at half maximum (FWHM), is evaluated as 3.87 mm, which is slightly degraded compared to the ideal spatial resolution

(2.88 mm). This is probably attributed to the estimated deviation of the optical fiber refractive index from its real value, or the narrowed actual optical range of the laser under 1 Hz scanning compared to that under a static state.

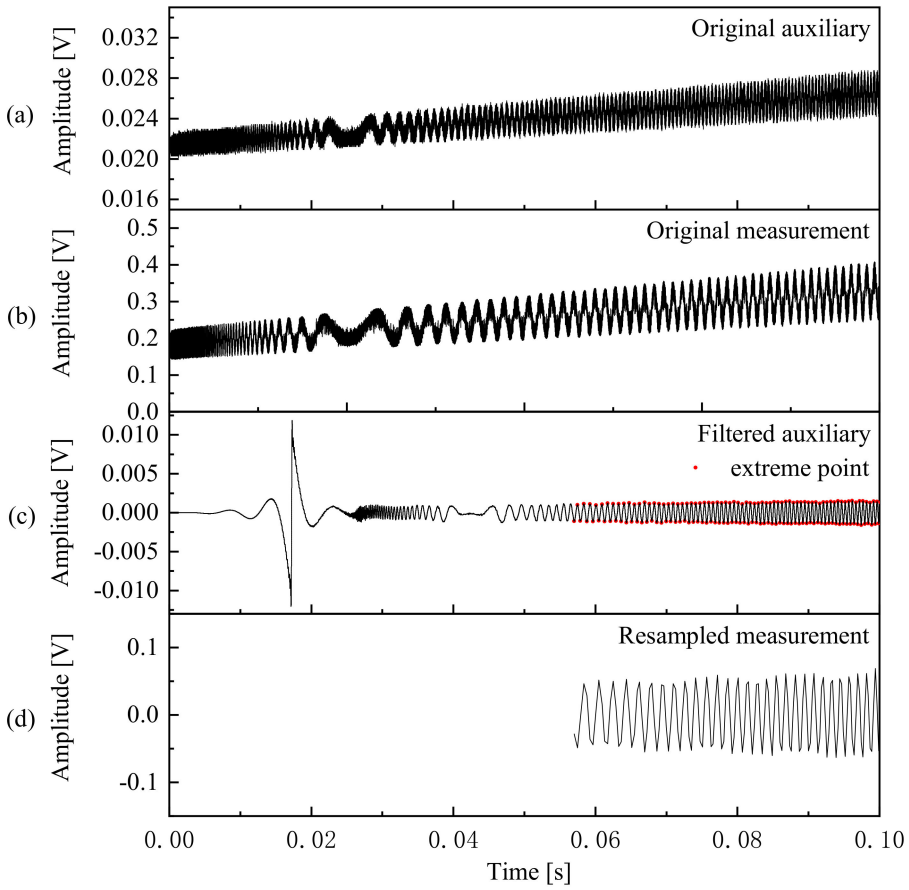

Figure 7. Interference signals. (**a**) Original auxiliary; (**b**) original measurement; (**c**) filtered auxiliary; (**d**) resampled measurement. Here, only a 0.1 s signal of the entire 1 s interference is demonstrated to show the signal characteristics more clearly.

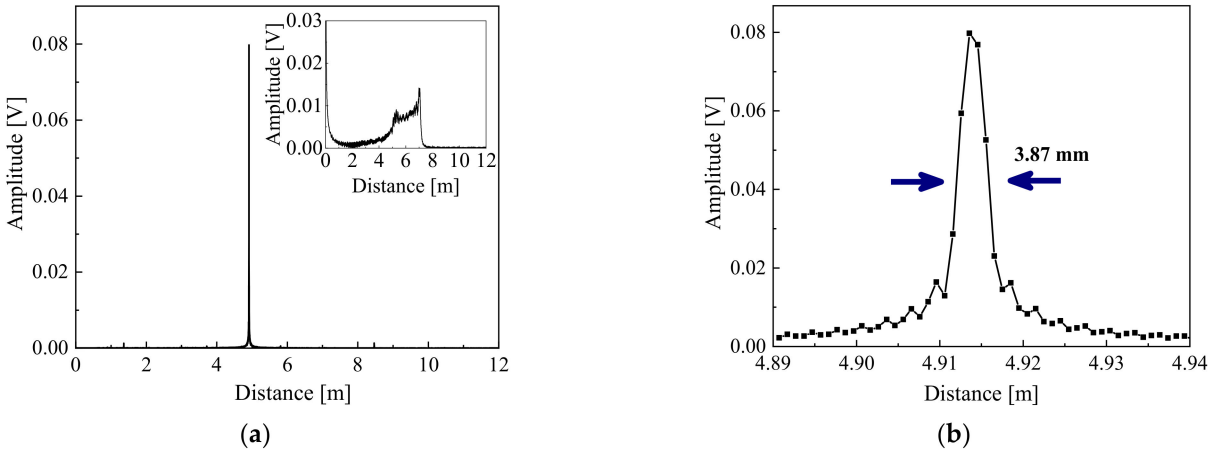

Figure 8. (**a**) Entire distance spectrum of the measurement interference signal. Inset: distance spectrum without frequency-resampling and filter processing. (**b**) Zoomed-in view of (**a**) around 4.9 m, showing a full width at half maximum of 3.87 mm.

To further evaluate the ranging performance of the sensor at different distances, optical delay fibers with different lengths were used to change the optical path difference of the measurement interferometer. The standard deviations of 20 measurements at different ranging distances are shown in Figure 9. It can be seen that the standard deviation of each distance is within 0.4 mm and relatively stable, indicating negligible fluctuation and excellent measurement repeatability.

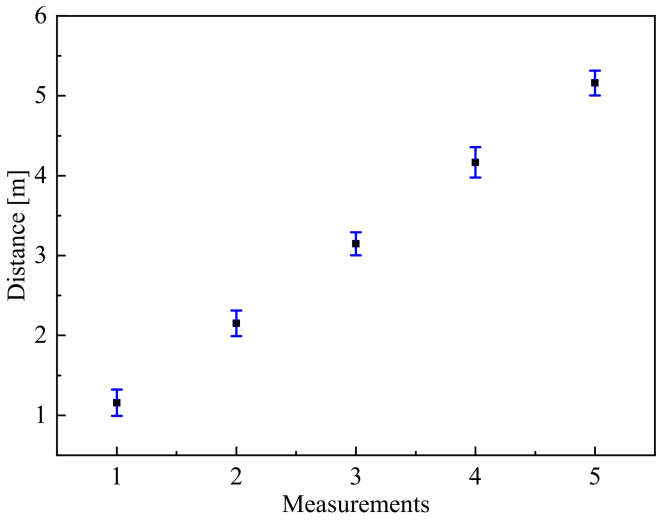

Figure 9. Standard deviation at different distances. Each error bar is the standard deviation from 20 measurements and the magnitudes of the error bars are scaled up by 500-fold for clarity.

5. Discussion

We have developed an all-fiber versatile PAS gas sensing technique by combining FMCW interferometry. The above results have demonstrated the capability of this proposed method for simultaneous measurement of gas concentration and location.

The current detection limit in gas concentration is only 28 ppm, which would limit many practical applications where ultrasensitive measurement is highly needed. As is known to all, the photoacoustic signal amplitude is proportional to the laser excitation power, that can be enhanced by power amplification [2,37], external cavity power enhancement [38], and laser internal cavity power enhancement [32] photoacoustic technologies. In addition, the sensitivity of the system critically relies on the property of the acoustic transducer, which can be improved by using more sensitive fiber-optical microphones [39,40] or quartz tuning forks (QTFs) [1,2,41] instead of conventional microphones. Furthermore, in the future, by integrating with the all-optical resonance photoacoustic sensor presented in [7], the system could achieve position resolved remote trace gas concentration.

For FMCW, in practical remote applications, a much longer sensing distance is needed. The maximum sensing distance is restricted by the optical difference of the auxiliary interferometer according to the Nyquist sampling law. However, the optical difference of the auxiliary interferometer can also be possibly limited by the sampling rate. A longer optical difference requires a higher sampling rate to obtain more accurate signal waveform. In this work, the auxiliary interferometer is 12 m, and the interference signal is sampled at 1 MS/s. If the sampling rate is improved to the GS/s level, it is expected that the sensing distance can reach several kilometers. In the case of remote sensing, another potential factor affecting the effective distance is the coherence length of the laser source, which is only ~100 m for our current laser source. A longer sensing distance can be expected by using a narrow linewidth laser [42] or compressing the laser linewidth [43,44]. Except distance, another parameter worth considering is the spatial resolution. Although the tuning nonlinear response has been compensated by implementing the frequency-resampling method to improve the spatial resolution, the achieved spatial resolution is still much worse than

the ideal one. This may be attributed to the DAQ delays or temporal jitter between the auxiliary interference signal and measurement interference signal during data digitization. This limitation could be further mitigated by using a delay line to repress the phase error by matching the two channels' path length [28]. Moreover, multipoint distance and gas concentration detection can be expected by adopting bus topology, in which multiple gas probes are distributed along a single backbone fiber in the measurement arm of the measurement interferometer [24].

6. Conclusions

We have demonstrated a versatile all-fiber sensing system by blending a fiber-pigtailed PAS sensor with an FMCW interferometer for simultaneous extraction of gas concentration and location. For gas concentration detection, wavelength modulation spectroscopy and 2*f* detection are used to measure the PAS signal. Experimental results demonstrate its excellent linear response to CH_4. The corresponding detection limit and NNEA are 28 ppm and 1.98×10^{-8} $cm^{-1} \cdot W \cdot Hz^{-1/2}$, respectively. For laser ranging, the auxiliary interferometer is used to resample the measurement interference signal at equal optical frequency intervals with mitigated influence of tuning nonlinearity. A Hanning window function digital band-pass filter and wavelet threshold denoising method are performed to denoise interference signals. The spatial resolution is experimentally assessed to be 3.87 mm within a distance range of 4.9 m. Moreover, several strategies for further improving the performance are discussed. Future work will focus on enhancing its capability of long-distance distributed detection in gas leakage detection or gas emission monitoring.

Author Contributions: Conceptualization, M.L. and Q.W.; methodology, M.H. (Mengpeng Hu) and M.L.; software, Q.W.; validation, M.H. (Mai Hu); formal analysis, H.Z., M.H. (Mai Hu) and T.T.; investigation, H.Z.; resources, Q.W. and J.W.; data curation, M.L.; writing—original draft preparation, M.L.; writing—review and editing, Q.W.; visualization, M.L. and M.H. (Mai Hu); supervision, Q.W.; project administration, Q.W.; funding acquisition, Q.W. and J.W. All authors have read and agreed to the published version of the manuscript.

Funding: This research was funded by the Second Comprehensive Scientific Investigation of the Qinghai-Tibet Plateau (2019QZKK020802), National Natural Science Foundation of China (NSFC) (62005267, 62005268), Strategic Priority Research Program of the Chinese Academy of Sciences (XDA17040513, XDA22020502), and Young Talent of Lifting Engineering for Science and Technology in Jilin, China (QT202106).

Institutional Review Board Statement: Not applicable.

Informed Consent Statement: Not applicable.

Data Availability Statement: The data that support the plots within this paper are available from the corresponding author on request.

Conflicts of Interest: The authors declare no conflict of interest.

References

1. Borri, S.; Patimisco, P.; Galli, I.; Mazzotti, D.; Giusfredi, G.; Akikusa, N.; Yamanishi, M.; Scamarcio, G.; De Natale, P.; Spagnolo, V. Intracavity quartz-enhanced photoacoustic sensor. *Appl. Phys. Lett.* **2014**, *104*, 091114. [CrossRef]
2. Ma, Y.; He, Y.; Zhang, L.; Yu, X.; Zhang, J.; Sun, R.; Tittel, F.K. Ultra-high sensitive acetylene detection using quartz-enhanced photoacoustic spectroscopy with a fiber amplified diode laser and a 30.72 kHz quartz tuning fork. *Appl. Phys. Lett.* **2017**, *110*, 031107. [CrossRef]
3. Lv, H.; Zheng, H.; Liu, Y.; Yang, Z.; Wu, Q.; Lin, H.; Montano, B.A.Z.; Zhu, W.; Yu, J.; Kan, R.; et al. Radial-cavity quartz-enhanced photoacoustic spectroscopy. *Opt. Lett.* **2021**, *46*, 3917–3920. [CrossRef]
4. Yin, X.; Dong, L.; Wu, H.; Gao, M.; Zhang, L.; Zhang, X.; Liu, L.; Shao, X.; Tittel, F.K. Compact QEPAS humidity sensor in SF_6 buffer gas for high-voltage gas power systems. *Photoacoustics* **2022**, *25*, 100319. [CrossRef]
5. Chen, K.; Zhang, B.; Liu, S.; Yu, Q. Parts-per-billion-level detection of hydrogen sulfide based on near-infrared all-optical photoacoustic spectroscopy. *Sens. Actuators B Chem.* **2019**, *283*, 1–5. [CrossRef]

6. Wang, Z.; Wang, Q.; Zhang, H.; Borri, S.; Galli, I.; Sampaolo, A.; Patimisco, P.; Spagnolo, V.L.; De Natale, P.; Ren, W. Doubly resonant photoacoustic spectroscopy: Ultra-high sensitivity meets ultra-wide dynamic range. *Photoacoustics* **2022**, *27*, 100387. [CrossRef]
7. Gong, Z.; Wu, G.; Jiang, X.; Li, H.; Gao, T.; Guo, M.; Ma, F.; Chen, K.; Mei, L.; Peng, W.; et al. All-optical high-sensitivity resonant photoacoustic sensor for remote CH_4 gas detection. *Opt. Express* **2021**, *29*, 13600–13609. [CrossRef]
8. He, Y.; Ma, Y.; Tong, Y.; Yu, X.; Peng, Z.; Gao, J.; Tittel, F.K. Long distance, distributed gas sensing based on micro-nano fiber evanescent wave quartz-enhanced photoacoustic spectroscopy. *Appl. Phys. Lett.* **2017**, *111*, 241102. [CrossRef]
9. Wei, T.; Zifarelli, A.; Dello Russo, S.; Wu, H.; Menduni, G.; Patimisco, P.; Sampaolo, A.; Spagnolo, V.; Dong, L. High and flat spectral responsivity of quartz tuning fork used as infrared photodetector in tunable diode laser spectroscopy. *Appl. Phys. Rev.* **2021**, *8*, 041409. [CrossRef]
10. Wu, H.; Dong, L.; Zheng, H.; Yu, Y.; Ma, W.; Zhang, L.; Yin, W.; Xiao, L.; Jia, S.; Tittel, F.K. Beat frequency quartz-enhanced photoacoustic spectroscopy for fast and calibration-free continuous trace-gas monitoring. *Nat. Commun.* **2017**, *8*, 15331. [CrossRef] [PubMed]
11. Wang, Q.; Wang, Z.; Ren, W. Wavelength-stabilization-based photoacoustic spectroscopy for methane detection. *Meas. Sci. Technol.* **2017**, *28*, 065102. [CrossRef]
12. Zhang, H.; Jin, W.; Hu, M.; Hu, M.; Liang, J.; Wang, Q. Investigation and Optimization of a Line-Locked Quartz Enhanced Spectrophone for Rapid Carbon Dioxide Measurement. *Sensors* **2021**, *21*, 5225. [CrossRef]
13. Yin, X.; Gao, M.; Miao, R.; Zhang, L.; Zhang, X.; Liu, L.; Shao, X.; Tittel, F.K. Near-infrared laser photoacoustic gas sensor for simultaneous detection of CO and H_2S. *Opt. Express* **2021**, *29*, 34258–34268. [CrossRef]
14. Aoyama, K.-I.; Nakagawa, K.; Itoh, T. Optical time domain reflectometry in a single-mode fiber. *IEEE J. Quantum Electron.* **1981**, *17*, 862–868. [CrossRef]
15. Eickhoff, W.; Ulrich, R. Optical frequency domain reflectometry in single-mode fiber. *Appl. Phys. Lett.* **1981**, *39*, 693–695. [CrossRef]
16. Sumida, S.; Okazaki, S.; Asakura, S.; Nakagawa, H.; Murayama, H.; Hasegawa, T. Distributed hydrogen determination with fiber-optic sensor. *Sens. Actuators B Chem.* **2005**, *108*, 508–514. [CrossRef]
17. Floridia, C.; Salgado, F.; Rosolem, J.; Bassan, F.; Fracarolli, J.; Penze, R.; Pereira, L. Methane leak detection and spectral analysis by using only optical time domain reflectometry in semidistributed remote optical sensors. In Proceedings of the 2016 IEEE SENSORS, Orlando, FL, USA, 30 October–3 November 2016; pp. 1–3. [CrossRef]
18. Jin, W.; Ho, H.; Cao, Y.; Ju, J.; Qi, L. Gas detection with micro-and nano-engineered optical fibers. *Opt. Fiber Technol.* **2013**, *19*, 741–759. [CrossRef]
19. Lin, Y.; Liu, F.; He, X.; Jin, W.; Zhang, M.; Yang, F.; Ho, H.L.; Tan, Y.; Gu, L. Distributed gas sensing with optical fibre photothermal interferometry. *Opt. Express* **2017**, *25*, 31568–31585. [CrossRef]
20. Stove, A.G. Linear FMCW radar techniques. In *IEE Proceedings F (Radar and Signal Processing)*; IET Digital Library: London, UK, 1992; Volume 139, pp. 343–350. [CrossRef]
21. Zavrsnik, M.; Stewart, G. Coherence addressing of quasi-distributed absorption sensors by the FMCW method. *J. Light. Technol.* **2000**, *18*, 57–65. [CrossRef]
22. Ye, F.; Qian, L.; Qi, B. Multipoint chemical gas sensing using frequency-shifted interferometry. *J. Light. Technol.* **2009**, *27*, 5356–5364. [CrossRef]
23. Lou, X.; Chen, C.; Feng, Y.; Dong, Y. Simultaneous measurement of gas absorption spectra and optical path lengths in a multipass cell by FMCW interferometry. *Opt. Lett.* **2018**, *43*, 2872–2875. [CrossRef]
24. Lou, X.; Feng, Y.; Chen, C.; Dong, Y. Multi-point spectroscopic gas sensing based on coherent FMCW interferometry. *Opt. Express* **2020**, *28*, 9014–9026. [CrossRef]
25. Miklós, A. Acoustic aspects of photoacoustic signal generation and detection in gases. *Int. J. Thermophys.* **2015**, *36*, 2285–2317. [CrossRef]
26. Dumitras, D.; Dutu, D.; Matei, C.; Magureanu, A.; Petrus, M.; Popa, C. Laser photoacoustic spectroscopy: Principles, instrumentation, and characterization. *J. Optoelectron. Adv. Mater.* **2007**, *9*, 3655. Available online: https://www.webofscience.com/wos/WOSCC/full-record/000251768700001 (accessed on 31 March 2022).
27. Glombitza, U.; Brinkmeyer, E. Coherent frequency-domain reflectometry for characterization of single-mode integrated-optical waveguides. *J. Light. Technol.* **1993**, *11*, 1377–1384. [CrossRef]
28. Moore, E.D.; McLeod, R.R. Correction of sampling errors due to laser tuning rate fluctuations in swept-wavelength interferometry. *Opt. Express* **2008**, *16*, 13139–13149. [CrossRef]
29. Shi, G.; Zhang, F.; Qu, X.-H.; Meng, X. High-resolution frequency-modulated continuous-wave laser ranging for precision distance metrology applications. *Opt. Eng.* **2014**, *53*, 122402. [CrossRef]
30. Ahn, T.-J.; Kim, D.Y. Analysis of nonlinear frequency sweep in high-speed tunable laser sources using a self-homodyne measurement and Hilbert transformation. *Appl. Opt.* **2007**, *46*, 2394–2400. [CrossRef]
31. Shi, G.; Wang, W.; Zhang, F. Precision improvement of frequency-modulated continuous-wave laser ranging system with two auxiliary interferometers. *Opt. Commun.* **2018**, *411*, 152–157. [CrossRef]
32. Wang, Q.; Wang, Z.; Chang, J.; Ren, W. Fiber-ring laser-based intracavity photoacoustic spectroscopy for trace gas sensing. *Opt. Lett.* **2017**, *42*, 2114–2117. [CrossRef]

33. Xuan, H.; Jin, W.; Liu, S. Long-period gratings in wavelength-scale microfibers. *Opt. Lett.* **2010**, *35*, 85–87. [CrossRef] [PubMed]
34. Stone, J.A.; Stejskal, A.; Howard, L. Absolute interferometry with a 670-nm external cavity diode laser. *Appl. Opt.* **1999**, *38*, 5981–5994. [CrossRef]
35. Baumann, E.; Deschênes, J.-D.; Giorgetta, F.R.; Swann, W.C.; Coddington, I.; Newbury, N.R. Speckle phase noise in coherent laser ranging: Fundamental precision limitations. *Opt. Lett.* **2014**, *39*, 4776–4779. [CrossRef] [PubMed]
36. Scherr, S.; Ayhan, S.; Fischbach, B.; Bhutani, A.; Pauli, M.; Zwick, T. Measurement. An efficient frequency and phase estimation algorithm with CRB performance for FMCW radar applications. *IEEE Trans. Instrum. Meas.* **2014**, *64*, 1868–1875. [CrossRef]
37. Wu, H.; Dong, L.; Zheng, H.; Liu, X.; Yin, X.; Ma, W.; Zhang, L.; Yin, W.; Jia, S.; Tittel, F.K. Enhanced near-infrared QEPAS sensor for sub-ppm level H_2S detection by means of a fiber amplified 1582 nm DFB laser. *Sens. Actuators B Chem.* **2015**, *221*, 666–672. [CrossRef]
38. Wang, Z.; Wang, Q.; Zhang, W.; Wei, H.; Li, Y.; Ren, W.J.O.L. Ultrasensitive photoacoustic detection in a high-finesse cavity with Pound–Drever–Hall locking. *Opt. Lett.* **2019**, *44*, 1924–1927. [CrossRef] [PubMed]
39. Mao, X.; Zheng, P.; Wang, X.; Yuan, S. Breath methane detection based on all-optical photoacoustic spectrometer. *Sens. Actuators B Chem.* **2017**, *239*, 1257–1260. [CrossRef]
40. Cao, Y.; Jin, W.; Ho, H.L.; Ma, J. Miniature fiber-tip photoacoustic spectrometer for trace gas detection. *Opt. Lett.* **2013**, *38*, 434–436. [CrossRef]
41. Hu, Y.; Qiao, S.; He, Y.; Lang, Z.; Ma, Y. Quartz-enhanced photoacoustic-photothermal spectroscopy for trace gas sensing. *Opt. Express* **2021**, *29*, 5121–5127. [CrossRef]
42. Wolf, E. *Introduction to the Theory of Coherence and Polarization of Light*; Cambridge University Press: Cambridge, UK, 2007.
43. Schibli, T.; Hartl, I.; Yost, D.; Martin, M.; Marcinkevičius, A.; Fermann, M.; Ye, J. Optical frequency comb with submillihertz linewidth and more than 10 W average power. *Nat. Photonics* **2008**, *2*, 355–359. [CrossRef]
44. Li, F.; Lan, T.; Huang, L.; Ikechukwu, I.P.; Liu, W.; Zhu, T. Spectrum evolution of Rayleigh backscattering in one-dimensional waveguide. *Opto-Electron. Adv.* **2019**, *2*, 19001201–19001207. [CrossRef]